CRYSTAL STRUCTURE INVESTIGATION OF FERRITIC 73FE24CR2SI0.8MN0.1NI STEEL FOR MULTI-PURPOSE STRUCTURAL MATERIAL APPLICATIONS

Parikin[1*], M. Dani[1], A.K. Jahja[1], R. Iskandar[2], J. Mayer[2]

[1]*Center for Science and Technology of Advanced Materials, BATAN, Kawasan Puspiptek, Serpong, Tangerang, Banten 15314, Indonesia*
[2]*Central Facility for Electron Microscopy (GFE), RWTH Aachen University, Ahorn strasse 55, D-52074 Aachen, Germany*

ABSTRACT

Microstructural identification of synthesized steel with significant local content has been carried out. Alloy ingot was prepared using a casting technique. The samples were then formed into bulk steel by a machining process. A high resolution powder neutron diffractometer (HRPD) was used as an equipment for characterization. By applying neutron diffraction techniques, a ferritic steel profile can be resulted in as well as 'minor peaks' belong to impurities formed in the sample. These impurities can be identified as small amounts of Al_2O_3 $54SiO_2$, Al_4C_3, SiC and $Cr_{23}C_6$. Scanning transmission electron microscopy (STEM) combined with energy dispersive X-ray spectroscopy (EDX) confirmed and revealed neutron identified phase distributions. Joint Committee on Powder Diffraction Standards (JCPDS) least square curves calibration can precisely calculate the d_{hkl} parameters of each reflection plane. As a comparison, another sample of alloy ingot was also investigated using neutron diffraction. The pattern was free from crystal impurities. Rietveld refinements provide satisfactory goodness of fits R_{wp} = 10.42% and reliability factor S = 1.7. This was so-called a 'real bulky' sample of a 73Fe24Cr2Si0.8Mn0.1Ni ferritic steel alloy.

Keywords: 73Fe24Cr2Si0.8Mn0.1Ni Steel; Crystal structure; Neutron diffraction; Transmission electron microscope

1. INTRODUCTION

An advanced nuclear system (Generation IV) has initially defined six advanced reactor concepts with the ability to greatly improve nuclear reactor performance in terms of safety, proliferation resistance, economic performance, and minimization of waste (NEA, 2013). Several improved alloy compositions have been developed and are being continuously developed for both austenitic and Ferritic-Martensitic (F/M) steels. Due to generating high temperatures, the reactor system may yield very high energy and supply high-temperature heat potensially used for massive hydrogen production through a water decomposition process.

Primary in-core structures are usually made of graphite and carbon-based ceramic composites, including the reactor pressure vessel (made of 2.25% Cr bainitic steel or 9% Cr martensitic steel) (Taban et al., 2012), cross vessel component, and intermediate heat exchangers that will divert heat from the primary side of the reactor to a hydrogen production plant. Such

*Corresponding author's email: farihin@batan.go.id, Tel: +62-21-7560922, Fax. +62-21-7560926

components place great demands on their construction materials. Therefore, mechanical strength, creep resistance and corrosion resistance are required for an extended lifetime (approximately 20 years). Additionally, thin wall sheets are subjected to temperatures up to 850 to 950°C and must sustain a differential pressure of 6 to 7 MPa during off-normal operations. Such temperatures demand the use of Ni-base alloys rich in chromium (about 22 %wt.) and strengthened by additions of molybdenum, cobalt, and tungsten. Improving nickel based alloys in high- temperature strength alloys would be clearly beneficial, but they have been limited by the type of applications, optimum design, and quality of the minerals (NEA, 2013).

Table 1 Chemical composition of 73Fe24Cr2Si0.8Mn0.1Ni ferritic steel

Element	Fe	Ni	Cr	Mn	Si	Al	Ti	Sn	Nb	C	S	P	V
%wt.	72.97	0.12	23.71	0.82	2.02	0.01	0.01	0.01	0.01	0.26	0.01	0.02	0.06

National Nuclear Energy Agency (BATAN)'s material engineers support the development of structural materials especially for reactor construction. A material with a significant local content has been synthesized, namely: the F1 type of alloy steel (Effendi et al., 2012). This alloy contains percentage weight of 73%Fe24%Cr2%Si 0.8%Mn0.1%Ni. Ferritic steel demonstrates the super alloy performance in hardness, corrosion resistance (Wahyono et al., 2015), and some mechanical properties. Laboratory-scale fabrication has been performed using casting methods (Kanthavela et al., 2014), to obtain a F1-ferritic alloy, a low carbon steel which is a non-standard chemical composition of elements, listed in Table 1 above. The purpose of synthesizing this ferritic steel is creating new ferritic types of materials with higher chromium content and reduced nickel content, thus the materials' corrosion resistance properties should be significantly improved. The steel is assumed to be an improved version of T91 and T92 (David et al., 2013) and is expected to be a candidate for use in the structural material of nuclear reactors.

The main objective of this research is focused on investigating the material quality of 73Fe24Cr2Si0.8Mn0.1Ni alloy steel. The scope of the observations is focused on crystal and microstructure characterizations obtained High Resolution Powder Neutron Difractometer (HRPD) and Transmission Electron Microscope (TEM) analyses.

2.   EXPERIMENTAL SETUP

First, the fractional quantities of each constituent component from the base materials were computed. Appropriate amounts of these base materials were weighed separately on the micro balance. The melting process used was similar to the A2 type steel casting technique explained in previous literature (Parikin et al., 2017). A mold made of silica-sand was constructed by mixing a bentonite binder with small amount of water. The finished mold was then lined with a specific material depending on the appropriate acid-, base-, or neutral environment. A neutral-type lining is a standard requirement if the desired product is stainless alloy. As a final step, the lining wall is sintered. Production of stainless steel requires a neutral environment, and this calls for an alumina (Al_2O_3) lining material used with a specific type of ramming binder. The ingot is then formed into bulk and finished via a machining process. Elemental compositions of the product materials are listed in Table 1 above. They were measured using a 1996 Swiss made Optical Emission Spectrometry (OES) that located in Polytechnique and Manufacture of Bandung. The equipment was employed in elemental composition measurements with the

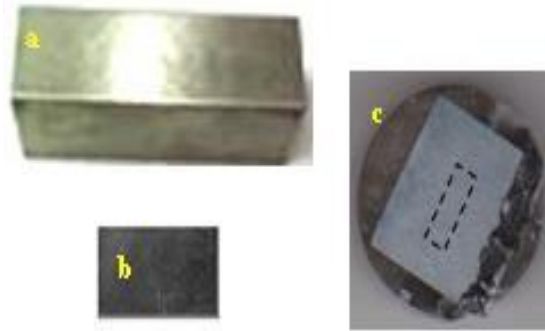sample specially prepared by the spark erosion method to produce a dimension of $2.5 \times 2.5 \times 12$ cm^3.

Figure 1 Macrostructures of 73Fe24Cr2Si0.8Mn 0.1Ni steel specimen: (a) a $2.5 \times 2.5 \times 12$ cm^3 specimen; (b) a $3.0 \times 2.0 \times 1.0$ mm^3 specimen prior to polishing-thinning; and (c) mounting specimen with a lamellae position to be dimple-grinded

For microstructures investigation, a standard procedure was followed. The characterization was accomplished by using a transmission electron microscope (TEM) and performed in Aachen Germany. The samples were prepared in five separate steps including using a Focused Ion Beam (FIB) (Dani et al., 2015) to form some small 15×0.1 μm^2 lamella specimens. The process was comprised of pre-preparing of the specimen, bounding, mounting, mechanical pre-thinning and final ion beam thinning. Figure 1 presents the macrostructures of the specimen used in this work. Test materials are in the form of a base metal of ferritic steel F1 type with the specimen dimension of: (a) for OES tests and neutron diffraction experiments; and (b-c) for TEM observations. The specimen for TEM observations (Kim et al., 2012) was initially pre-prepared by slicing it into $3.0 \times 2.0 \times 1.0$ mm^3 pieces using a diamond wafering machine. The 15×0.1 μm^2 lamella square was thinned down to approximately <100 nm by an ion beam prior to being inserted into the system's sample vacuum chamber. Meanwhile, the crystal structure was measured by collecting reflection intensities using a neutron diffractometer and refined by Rietveld method. High resolution powder diffractometer (HRPD-1.82 Å) utilizes neutrons as a source, has 32 high sensitive detectors that capable of simultaneously measuring the diffraction patterns of a compound. This device is an excellent non-destructive tool for characterizing the material's crystal structures since it utilizes neutrons that have higher penetrating power than X-rays. In most engineering materials, neutron diffraction is the preferred method for measuring bulk crystal structures. This allows the thermal neutrons beam scattered from the reactor to deeply analyze the structure of a thick material by a simple preparation. Therefore, a complete set of experimental data would be obtained by this method.

3. RESULTS AND DISCUSSION

3.1. Neutron Diffraction Profiles

Figure 2 shows the neutron diffraction pattern using a wavelength of 1.82 Å. The measured experimental diffraction pattern of the steel specimen was of excellent or high quality. The peak to background ratio is adequate and one is still able to distinguish between real diffraction peaks and the chopped background. The entire diffraction pattern shows four dominant diffraction peaks, which is typical for a body-centered tetragonal (bct) crystal system (Woo et al., 2015). Successive peaks in the diffractogram in order of appearance are the (110), (200), (211) and (220) planes. These planes are numerically grouped by alternating between odd and even numbers, which are diffracted at consecutive 2θ-angle of 53.30°, 78.74°, 101.94° and 127.56° respectively. However, the diffraction pattern is a mixture of standard and

unidentified minor peaks which can inflate the background counts. Parts of these diffraction peaks were clearly scanned at 2θ measurement angles ranging from 5° to 135°. These unidentified peaks could originate from undesirable contaminants and are an obstacle to the refinement process. It was very difficult to achieve the convergence of accurate calculations in the refinements.

Neutron diffractogram data in Figure 2 must be corrected to improve the diffraction pattern. Minor peaks in the diffraction pattern of the Rietan '94 program's calculation were usually not taken into considerations (excluded) to obtain reference number values or goodness of fit (R_{wp}; S). Otherwise, unidentified peaks may be predicted via the Bragg formula to obtain the d_{hkl} of -crystal elements or compounds in the material. First, the calibration equations have to be manually formed by correlating the $2 \sin \theta / \lambda$ and $1/d_{hkl}$, from the crystallographic data to find a line equation using the least square method.

The equation was then utilized to calculate the d_{hkl} of a certain peak belonging to the crystal elements or compounds. Secondly, software packages or codes are used to perform the 'search and match' process to estimate the yet unidentified reflection peaks of crystal elements or compounds present in the diffraction pattern.
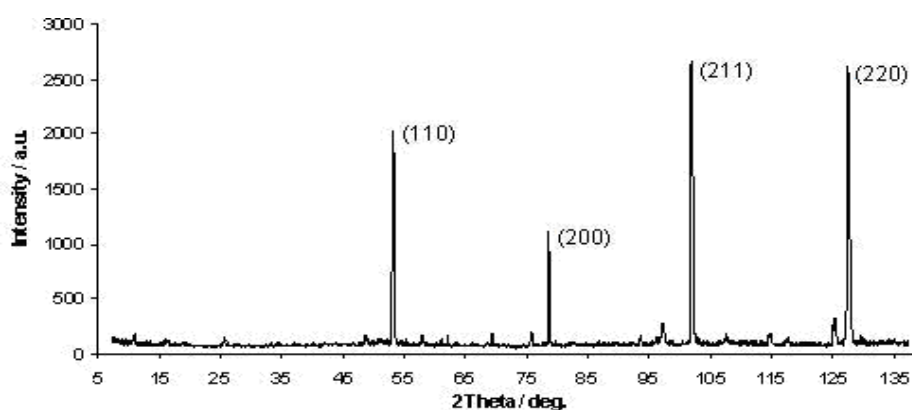

Figure 2 A Neutron diffraction profiles of 73Fe24Cr2Si 0.8Mn0.1Ni ferritic steel specimen from a High Resolution Powder Diffractometer (HRPD-1.82Å)

Table 2 Crystal structure parameters of 73Fe24Cr2Si 0.8Mn0.1Ni ferritic steel

Crystallography of F1-Type Steel		
Formula	:	Fe
Space Group	:	I4/mmm (I-139)
Lattice Parameters: a (Å)	:	2.866
b (Å)	:	2.866
c (Å)	:	2.874
α, β, γ (deg.)	:	90,90,90
Volume Cell (Å^3)	:	23.607
Number of Atoms/unit cell, Z	:	2
Atomic Positions $x, y\, z$	:	0.0 0.0 0.0

Initial crystallographic parameters for Rietveld refinement are compiled in Table 2 (Parikin et al., 2009). The listed crystallographic data was used as initial data in the process of refinements by the Rietveld method (Kumar et al., 2015). Data analysis was performed with the Rietan-94 program to compute the powder diffraction data obtained by X-ray and neutron method. Each operation was running well. This program takes the initial crystallographic data and form the pattern of the model and scanning neutron scattering chopped test specimens forms the

standard pattern. In Rietveld refinement, least squares is performed until convergence is achieved (best fitting) between all the observed diffraction patterns and the entire pattern of the intensity calculation. This calculation is based on the simultaneous smoothing models and other characteristics such as lattice parameters, the effect of optical diffraction, and factor modeling the desired appropriate instrument. Key to the solution is the feedback for smoothing, between a working knowledge of the structure and allocation of the Bragg reflection intensity observations of individual mutually overlapping portions (Parikin et al., 2013). Figure 3 displays the pattern for a single-phase Rietveld refinement of the steel specimen. In the diagram, there are signs of line broadening such some vertical lines under standard patterns and models. The lines indicate the position of the phase in steel specimens of 73Fe24Cr2Si0.8Mn0.1Ni. A full pattern of a standard profile and refinement is successively displayed in the diagram.

Smoothing results clearly show the crystalline symmetry belongs to the body centered tetragonal (bct) crystal system. In the diagram the reflection planes of (110), (200), (211), and (220) are patterned by mixing even and odd numbers. There is evidence of other phases (small peaks) in the range of the specimen's diffraction patterns. It can be assumed for the entire diffraction zone that the crystal consists of a mixture of the total pattern of a body-centered tetragonal and some small peaks of impurities. Refinement was performed using single-phase models, namely the ferritic phase (αFe) with space group I4/mmm (I-139) which is given in Table 2.
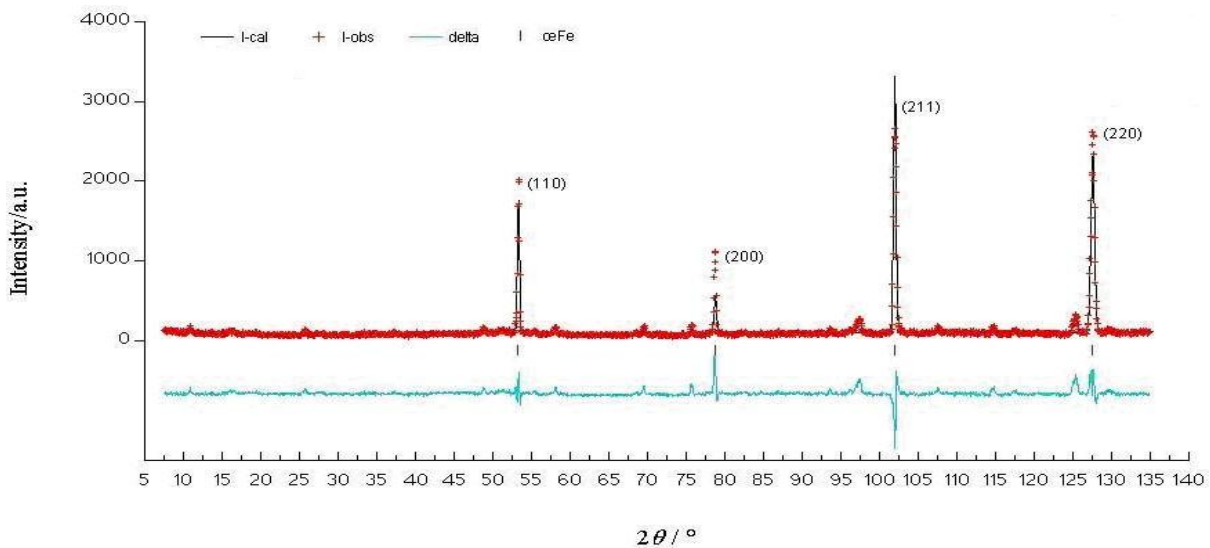

Figure 3 Rietveld refinement pattern of 73Fe24Cr2Si 0.8Mn0.1Ni ferritic steel specimen from HRPD-1.82 Å

The profile shape of the peak was modeled separately using the pseudo-Voight function which is a linear combination of Gaussian and Lorentzian functions. To make the angular data acquisition experimental results reliable, the structural phase parameters are then refined. The refined parameters are the lattice parameter, isotropic thermal parameter, deviation of the zero-point, preferred orientation (anisotropic), and the profile parameters (Gauss-Lorentz). Smoothing phase models are not quite satisfactory with a weighted-profile reliability factor (Rwp) value of 20% and a reliability factor S of 2. The residual appears to be a coarse line with very noisy peaks. The values still have a somewhat low statistical probability due to obstructions in the process of data fitting and significant interference by some unidentified peaks. So, it is very difficult for the refinement process to achieve good convergence (see Figure 3).
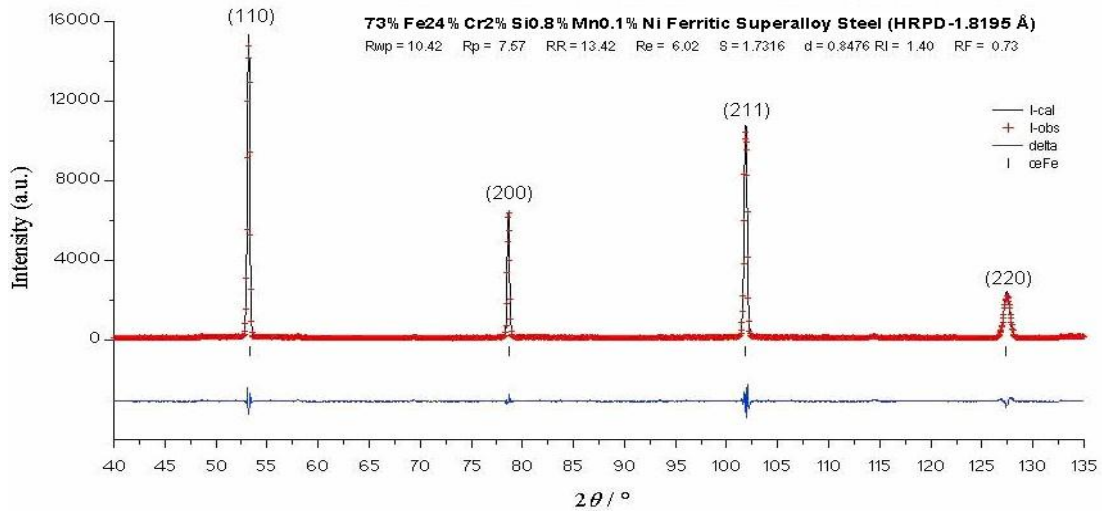
Figure 4 Rietveld refinement pattern of "real bulky" 73Fe 24Cr2Si0.8Mn0.1Ni ferritic steel specimen from high resolution powder diffractometer HRPD-1.82 Å

In comparison with the results of other neutron diffraction measurements of mechanically 'real bulky' specimens of 73Fe24Cr2Si0.8Mn0.1Ni ferritic steel, it is shown in Figure 4 that the overall reflection profile was free from impurities. Rietveld refinements (Pereira et al., 2015; Frølich et al., 2016; Bella & Henderson, 2016) give a quite satisfactory goodness of fits factor, reaching the weighted-profile R-factor R_{wp} value of 10.42% and reliability factor S of 1.7. The Residual profile seems to be a straight-line with a minuscule ripple at each peak position.
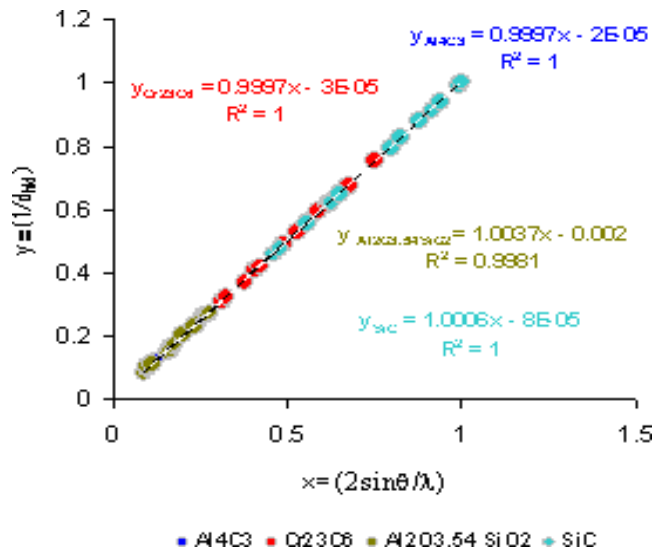

Figure 5 Least square curves calibration for identification of $Al_2O_354SiO_2$, Al_4C_3, $Cr_{23}C_6$ and SiC in a 73Fe24Cr2Si 0.8Mn0.1Ni ferritic steel specimen

3.2. Least Square Approximations

In addition to the principal peaks belonging to the *bct* structure of the 73Fe24Cr2Si0.8Mn0.1Ni ferritic super alloy steel, there are some unknown or unidentifiable peaks in the diffraction pattern. Based on the results of Rietveld refinements, the goodness of fit (R_{wp};S) factor is not quite satisfactory. The refined parameter values turned out to be difficult to converge to a minimum due to the presence of some unidentified peaks in the measured diffraction pattern. Identification of these peaks can be performed manually by evaluating the d_{hkl} spacings.

A simple calculation of d_{hkl} was performed by applying the Bragg formula (Humphreys, 2013) $\lambda = 2d_{hkl} \sin\theta$ by correlating $(1/d_{hkl})$ with $(2\sin\theta/\lambda)$ in the least square method. In the beginning, verification or confirmation of the crystallographic data, 2θ and d_{hkl} of Al2O3.54 SiO2 (44-0003), Al_4C_3 (35-0799), $Cr_{23}C_6$ (35-0783) and SiC (42-1360) -were taken from JCPDS database (JCPDS, 2014) to find the liniear equation of $x = (2\sin\theta/\lambda)$ versus $y = (1/d_{hkl})$. Then, equations were utilized to compute the d-spacing of the obtained 2θ peaks. It was found that correlations of the linear equations are strong enough, resulting in a χ-square (R^2) close to unity (~1). Furthermore, the identified minor peaks belong to aluminum silicate $(Al_2O_3.54SiO_2)$ with an orthorhombic structure, space group Pnma (I-62), and lattice parameter a = 20.10 Å, b = 19.89 Å and c = 13.39 Å, then aluminum carbide (Al_4C_3) with fcc structure, space group Fm3m (I-225), lattice parameter of a = b = c = 10.65 Å, also silicon carbide (SiC) with tetragonal structure, space group $P6_{3mc}$ (I-186), lattice parameter a = b = 3.08 Å and c = 10.06 Å and chromium carbide $(Cr_{23}C_6)$ with bct structure, space group Rǯm (I-225), lattice parameter of a = b = 3.338 Å and c = 24.99 Å as graphically in Figure 4. The d-spacing of crystals was evaluated via the least squares method by obtaining the linear equations of $y(Al_2O_3.54 SiO_2) = 1.0037x-0.002$, then $y(Al_4C_3) = 0.9997x- 0.00002$, $y(Cr_{23}C_6) = 0.9997x–0.00003$ and $y(SiC) = 1.0006x-0.00008$ respectively.

A few obtained *d*-spacings tend to overlap with one another to make a straight-line; starting from aluminum silicate, aluminum carbide, chromium carbide and finally silicon carbide (see Figure 5). Table 3 lists some *d*-spacings of the small or weak peaks conforming with the JCPDS data.

Table 3 Some *d*-spacing of the minor peaks conforming with the JCPDS database

Formula	2θ (°)	Plane			Relative Intensity	d-spacing (Å)	
		h	*k*	*l*		LS*	JCPDS
$Al_2O_3.54SiO_2$	10.88	1	1	1	17	9.71	9.68
	16.20	3	0	1	11	6.37	6.34
	18.10	0	3	1	5	5.95	5.92
	25.75	0	1	8	10	4.15	4.16
	51.38	0	0	12	49	2.09	2.08
Al_4C_3	58.14	1	0	10	23	1.89	1.89
	69.52	1	0	13	<1	1.61	1.60
	75.70	0	1	14	18	1.50	1.51
	75.70	6	4	0	<1	1.48	1.48
	93.60	8	2	2	12	1.25	1.25
	97.38	6	6	2	15	1.22	1.21
$Cr23C_6$	107.57	9	3	1	1	1.12	1.11
	114.68	8	4	4	6	1.08	1.09
	117.38	7	7	1	3	1.06	1.07
	125.35	10	2	2	1	1.02	1.02
SiC	51.38	0	0	6	10	2.09	2.09
	58.14	0	0	7	20	1.86	1.87
	69.52	1	0	19	10	1.60	1.59
	75.70	1	1	0	90	1.47	1.48
	93.60	0	0	10	40	1.25	1.24
	97.38	2	0	2	10	1.20	1.20
	107.57	1	0	10	20	1.13	1.13
	114.68	2	0	8	40	1.09	1.08
	117.38	2	0	7	10	1.06	1.06
	125.35	1	0	34	10	1.01	1.02
	129.52	2	1	0	50	1.00	1.00

*Least Square

3.3. Microstructures

Figure 6 shows the un-machined surface specimen (longitudinal direction) with a magnification of 5000× using FIB-SEI (Focused Ion Beam - Scanning Electron Image). A micrograph was

concentrated on which the lamellae will be taken into the FIB system (Burnett et al., 2016). It can be seen as a rectangle in Figure 6a. It is observed that much coagulation in the steel materials is exposed. The solid solution process was not perfect enough. Pores and cracks are distributed across the whole surface. Some parts of the surface might not be heated or cooled uniformly during the fabrication process. Non-metallic elements contribute to pores and cracks formation in the surfaces. It is found that silicates and carbides such as: aluminum silicate, aluminum carbide, and chromium carbide are present in the investigated areas. It is very clear that the microstructure exhibits coagulated grains caused by different rates of rapid cooling during fabrication.

Previous reports (Effendi et al., 2012; Effendi et al., 2014) revealed the outer density of the material is lower than the inner density due to pores and cracks forming in the material's surface (see Figure 6b). For this reason, mechanical treatments must be carried out until about 3.5 μm in depth is reached by machining process to find the compact surface of the 'real bulky' steel. Figure 6b shows a TEM image of about a 3.5μm cross section depth (transversal direction) from the surface of the 73Fe24Cr2Si0.8Mn0.1Ni ferritic super alloy steel. The image delineates pore thickness until about 3 μm in depth close to the real surface of the steel. The density of materials clearly traced from upper to beyond the real surface via grey color degradation. It should be understood that silicate has amorphous structures. So, aluminum silicate and silicon carbide have no dense structures compared to aluminum carbide and chromium carbide. Their mass densities are lighter than that of iron-carbon (Fe-C). They tend to move to the upper layers, occupying the outer surface. It was observed that these compounds are partly found on the top of surfaces.

Figure 6 (a) FIB-SEI on surface of 73Fe24Cr2Si0.8Mn0.1Ni steel; (b) TEM image on depth of surface 3.5 μm of 73Fe24Cr2Si0.8Mn0.1 Ni steel

Aluminum and oxygen were covering the pores of samples, forming the delta (δ) structures with silicon and carbon in the pore surface. Meanwhile, silicon, carbon, and oxygen content beyond the pore surface are overlap high enough with silicon artifact signals caused by tungsten and carbon protective layers, respectively. Generally, corrosive atmospheres and high temperature environments may attack the material's surface. The presence of these elements may be risky due to interacting with others by forming oxides, thus causing corrosion. Weakened material usually starts from this side due to the presence of micro-crystal stresses (Parikin et al., 2013). It might further initiate intergranular cracks and be able to migrate slowly and rapidly among the grain boundaries. However, it is clearly seen in Figure 5a that pores and cracks are widely spread on the entire area of the sample surface. It may be reasonably presumed that the solid solution cooling process of the molten metal occurs very fast. It creates

many air bubbles which are trapped in almost the entire range of the surface. This may increase the values of micro-crystal stress in the material.

3.4. EDX Mapping

Processing the TEM image capture was carried out by using a secondary electron detector (SEI) on the acceleration energy of the primary electron beam source emerged from tungsten wire by a maximum of 200 keV while the working distance (WD) was kept constant at 100 nm. The WD value is setup to obtain the EDX spectrum in the best condition. EDX was taken on the dead time value on average between 20 and 40% (Dani et al., 2015). The EDX spectrum of the specimen taken around the Fe-C stripe surface is shown in Figure 6. The spectra concentrated on the area of the specimen wherever there are pores/semi-pores and cracks. Higher magnifications of one pore area strip on Fe-C maps are artifacts from the EDX system. It was observed in the pores/semi- pores and in the cracks containing high carbon and oxygen. High oxygen concentrations and some amount of alumina are found in the pores. Pore areas at the lower part of the lamella (3 μm below the surface) are surrounded by chromium. Moreover, strong diffractions contrasted on the STEM-EDX image showed defects and dislocations (Harjo et al., 2016) were formed only up to 3 μm below to the surface.
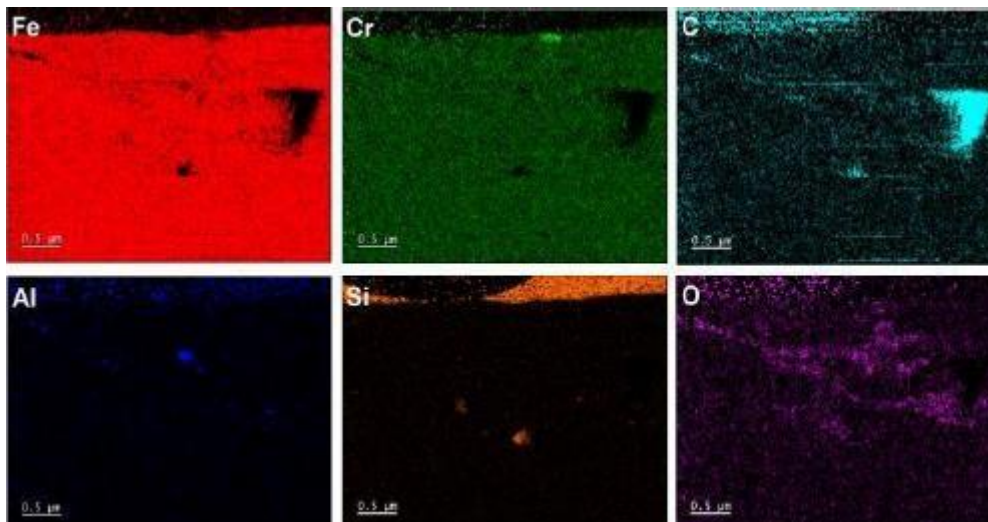

Figure 7 EDX maps on 0.5 μm surface depth of 73Fe24Cr2Si0.8Mn0.1Ni ferritic steel specimen

EDX semi quantitative maps show the concentration of each identified elements (in percentage weight). The percentage of carbon content detected in the surface specimen ranges from about 55 % to 64 % (Dani et al., 2017). This finding seems to conform with the microgram shown in Figure 7. The carbon element is distributed from outer to inner surface. So, it seems the carbon elements migrate via grain boundaries from the inner to outer surface, accumulating at pores and cracks. Fe and Cr elements tend to have a constant mass fraction. However, there was an interesting phenomenon of Si, C, and Al elements emerging from the surface metal areas in the form of aluminum silicate, aluminum carbide, silicon carbide, and chromium carbide compounds. The additional fraction of these elements may be the coagulation of 'migrant' elements, diffusing into a certain enriched site while other locations remain deficient of these specific elements. The presence of aluminum silicate in the sample, may be explained as alumina (Al_2O_3) and silicon (Si) leftover which are used in the sample preparation.

4. CONCLUSION

In summary, there are some 'impurity' compounds, as evidenced by the unidentified reflections in the measured neutron diffractogram. The neutron diffraction techniques revealed, in addition

to the ferritic steel profile, some minor peaks which belong to impurities formed in the sample. These impurities can be identified as a small amount of Al_2O_3 $54SiO_2$, Al_4C_3, SiC, and $Cr_{23}C_6$. Scanning transmission electron microscopy (STEM) combined with energy dispersive X-ray spectroscopy (EDX) analyses confirmed and revealed the neutron identified phase distributions. JCPDS least square curves calibration can precisely calculate the d_{hkl} parameters of each reflection plane of impurities. As a comparison, another specimen taken from the middle of an alloy-ingot was also investigated by neutron diffraction. The pattern was free from crystal impurities. Rietveld refinements give a satisfactory goodness of fit R_{wp} = 10.42% and reliability factor S = 1.7. This was then called a 'real bulky' sample of 73Fe24Cr2Si0.8Mn0.1Ni ferritic steel alloy.

5. ACKNOWLEDGEMENT

6. REFERENCES

Bella, A.M.T., Henderson, C.M.B., 2016. Rietveld Refinement of the Crystal Structures of $Rb_2XSi_5O_{12}$ (X = Ni, Mn). *Crystallographic Communications*, Volume 72, pp. 249–252

Burnett, T.L., Kelley, R., Winiarski, B., Contreras, L., Daly, M., Gholinia,, A., Burke, M.G., Withers, P.J., 2016. Large Volume Serial Section Tomography by Xe Plasma FIB Dual Beam Microscopy. *Ultramicroscopy*, Volume 161, pp. 119–129

Dani, M., Parikin, Iskandar, R., Dimyati, A., 2017. Investigation on Precipitations and Defects of the Fe-24Cr-2Si-0.8Mn Ferritic Super Alloy Steel. *Indonesian Materials Science Journals* (Jurnal Sains Materi Indonesia), Volume 18(4), pp. 173–178

Dani, M., Untoro P., Putra T.Y.S.P., Parikin, Mayer, J., Dimyati, A., 2015. Transmission Electron Microscopy Characterization of High-temperature Oxidation of Fe-20Cr-5Al Alloy Prepared by Focused Ion Beam Technique. *Makara Journal of Technology*, Volume 19(2), pp. 85–89

David, S.A. , Siefert, J.A., Feng, Z., 2013. Welding and Weldability of Candidate Ferritic Alloys for Future Advanced Ultra Supercritical Fossil Power Plants. *Science and Technology of Welding and Joining*, Volume 18(8), pp. 631–651

Effendi, N., Darwinto, T., Ismoyo, A.H., Parikin, 2014. 24-Chromium Ferritic Steel Magnetic Properties. *Indonesian Materials Science Journals* (Jurnal Sains Materi Indonesia), Volume 15(4), pp. 187–191

Effendi, N., Jahja, A.K., Bandriana, Adi, W.A., 2012. Some Data of Second Sequence non Standard Austentic Ingot A2. *Urania, Scientific Journal of Nuclear Fuel Cycle*, Volume 18(1), pp. 48–58

Frølich, S., Leemreize, H., Jakus, A., Xiao, X., Shah, R., Birkedal, H., Almer, J.D., Stock, S. R., 2016. Diffraction Tomography and Rietveld Refinement of a Hydroxyapatite Bone Phantom. *Journal of Applied Crystallography*, Volume 49(1), pp. 103–109

Harjo, S., Kawasaki, T., Gong, W., Aizawa, K., 2016. Dislocation Characteristics in Lath Martensitic Steel by Neutron Diffraction. *Journal of Physics: Conference Series* Volume 746, pp. 1–7

Humphreys, C.J., 2013. The Significance of Bragg's Law in Electron Diffraction and Microscopy, and Bragg's second law. *Foundations of Crystallography, Acta Crystallography*, Volume A(69), pp. 45–50

JCPDS (Joint Committee on Powder Diffraction Standards), 2014. *International Centre for Diffraction Data, PCPDFWIN, PDF-2 Powder Diffraction File, Release 2014*. Cambridge University Press, USA

Kanthavela, K., Arunkumar, K., Vivek, S., 2014. Investigation of Chill Performance in Steel Casting Process using Response Surface Methodology. *Procedia Engineering*, Volume 97, pp. 329–337

Kim, H.J., Choi, S.H., Bae, H.B., Lee, T.W., 2012. Transmission Electron Microscopy (TEM) Sample Preparation of Si1–xGex in c-Plane Sapphire Substrate. *NASA STI Program*, pp.1–29

Kumar, V., Kumari, S., Kumar, P., Kar, M., Kumar, L., 2015. Structural Analysis by Rietveld Method and its Correlation with Optical Propertis of Nanocrystalline Zinc Oxide, Advanced. *Materials Letters*, Volume 6(2), pp. 139–147

NEA (Nuclear Energy Agency), 2013. *Status Report on Structural Materials for Advanced Nuclear Systems, Nuclear Energy Agency Organisation for Economic Co-operation and Development*. Available online at http://www.oecd-nea.org/science/pubs/2013/6409-sr-mans.pdf, Accessed on October 27, 2017

Parikin, Bandriyana, Wahyono, I., Ismoyo, A.H., 2013. Non-destructive Residual Stress Analysis around the Weld-joint of Fuel Cladding Materials of ZrNbMoGe Alloys. *Atom Indonesia Journals*, Volume 39(2), pp. 65–74

Parikin, Ismoyo, A.H., Dimyati, A., 2017. Residual Stress Measurements on the TIG Weld Joint of 57Fe15Cr25Ni Austenitic Steel for Structural Material Applications by Means X- Ray Diffraction Techniques. *Makara Journal of Technology*, Volume 21(2), pp. 49–57

Parikin, Killen, P., Rafterry, A., 2009. Measurements of Residual Stresses in Cold-Rolled 304 Stainless Steel Plates using X-ray Diffraction with Rietveld Refinement Method. *Atom Indonesia Journals*, Volume 35(1), pp. 19–36

Pereira, P.F.S., Nogueira, I.C., Longo, E., Nassar, E.J., Rosa, I.L.V., Cavalcante, L.S., 2015. Rietveld Refinement and Optical Properties of SrWO4:Eu3+ Powders Prepared by the Non- hydrolitic Sol-Gel Method. *Journal of Rare Earths*, Volume 33(2), pp. 113–128

Taban, E., Kaluc, E., Atici, T., Kaplan, E., 2012. 9-12% Cr Steels: Properties and Weldability Aspects, the Situation in Turkish Industry. *In:* Proceeding of the 2nd International Conference on WeldingTechnologies and Exhibition. Ankara-Turkey, pp. 203–212

Wahyono, I., Salam, R., Parikin, Dimyati, A., 2015. Characterisation of Microstructures By using SEM and XRD on Corrosion Resistant of SS430 Commercial Steel and F1 non Commercial Steel. *In:* Prosiding Seminar Nasional XI SDM Teknologi Nuklir (Indonesian National Seminar XI SDM Nuclear Technology*)*, pp.112–117

Woo, W., Huang, E.W., Yeh, J.W., Choo, H., Lee, C., Tu, S.Y., 2015. In-situ Neutron Diffraction Studies on High-temperature Deformation Behavior in a CoCrFeMnNi High Entropy Alloy. *Intermetallics*, Volume 62, pp. 1–6